Magnetosheath Jet Interaction with the Magnetopause: Results from the 3D hybrid-kinetic Simulation Amitis

Eva Krämer,[1★] Shahab Fatemi,[1] Herbert Gunell,[1], Maria Hamrin,[1], Adrian Pöppelwerth,[2] and Niklas Grimmich[2,3]
[1]*Department of Physics, Umeå University, Umeå, Sweden*
[2]*Institut für Geophysik und Extraterrestrische Physik, Technische Universität Braunschweig, Braunschweig, Germany*
[3]*Department of Space Physics, Institute of Atmospheric Physics Czech Academy of Sciences, Prague, Czechia*

Accepted XXX. Received YYY; in original form ZZZ

ABSTRACT

The magnetopause marks the boundary where the pressure of the magnetosheath balances the magnetic pressure of Earth's magnetic field. Localized increases in magnetosheath pressure can therefore displace the magnetopause. One known plasma structure that exhibits such a local pressure increase is magnetosheath jets defined as transient dynamic pressure enhancements. These jets are particularly prominent downstream of the quasi-parallel bow shock, where they frequently interact with the magnetopause. To investigate the spatial and temporal characteristics of these interactions, we employ the 3D hybrid-kinetic plasma model Amitis with a steady plasma inflow. Our results show that jets downstream of the quasi-parallel bow shock can generate magnetopause surface waves that propagate flankward. Interestingly, while jets appear to have a similar velocity as the surface waves and continuously drive them, the jets apparent flankward motion does not align with the ion bulk velocity measured within the jets. This discrepancy may suggest ongoing jet generation at the bow shock, potentially linked to foreshock compressive structures.

Key words: Earth – plasmas – methods: numerical

1 INTRODUCTION

The Earth's magnetopause acts as a boundary between the solar wind, a continuous plasma outflow from the Sun, and the Earth's magnetic field. Its stand-off distance is primarily governed by the pristine solar wind dynamic pressure and the B_z component of the interplanetary magnetic field (IMF) (e.g. Shue et al. 1997; Chao et al. 2002; Sibeck et al. 1991). Upstream of the magnetopause, the bow shock decelerates, thermalizes, and deflects the solar wind plasma, forming the magnetosheath, a turbulent region of compressed solar wind plasma. Within the magnetosheath, localized dynamic pressure enhancements, known as magnetosheath jets, are frequently observed (e.g. Archer & Horbury 2013; Plaschke et al. 2013, 2018; Krämer et al. 2025b). These jets can locally deform the magnetopause due to their enhanced dynamic pressure, causing transient magnetopause boundary motions (Amata et al. 2011; Shue et al. 2009; Hietala et al. 2012; Escoubet et al. 2020; Ma et al. 2024; Archer et al. 2012).

Traditionally, jets have often been considered isolated, cylindrical structures (Archer et al. 2012; Plaschke et al. 2016; Karlsson et al. 2012), implying spatially confined interactions with the magnetopause (Norenius et al. 2021; Krämer et al. 2025). However, recent studies challenge this view, indicating that jets are often complex, interconnected, and dynamically evolving structures (Fatemi et al. 2024; Ren et al. 2024). These findings suggest that the interaction with the magnetopause might be more complex than previously suggested and needs therefore further investigation.

Magnetosheath jets can occur under all IMF conditions, but their occurrence rate is strongly influenced by the angle between the IMF and the bow shock normal, θ_{Bn} (Vuorinen et al. 2019; Plaschke et al. 2013). When $\theta_{\mathrm{Bn}} < 45°$, the bow shock is considered quasi-parallel; for $\theta_{\mathrm{Bn}} > 45°$, it is quasi-perpendicular. Likewise, the magnetosheath downstream of the shock can be classified as quasi-parallel and quasi-perpendicular. The dynamics of these two regimes differ significantly due to the presence of reflected particles upstream of the quasi-parallel shock, forming the foreshock region (Eastwood et al. 2005; Karlsson et al. 2021). Jets are observed approximately nine times more frequently downstream of the quasi-parallel shock than the quasi-perpendicular shock (Vuorinen et al. 2019), and their formation is therefore often linked to processes occurring at the quasi-parallel bow shock and in the foreshock region.

Several formation mechanisms have been proposed for jet generation. For example, Hietala & Plaschke (2013) linked jets to localized inclinations of the bow shock (bow shock ripples), while Raptis et al. (2022a) proposed that continuous shock reformation contributes to jet formation. Using simulations instead of spacecraft observations, Suni et al. (2023, 2021) suggested that compressive foreshock structures are the primary source of jets downstream of the quasi-parallel shock while Omelchenko et al. (2021) proposed a magnetokinetic formation mechanism, tying the generation to the highly fluctuating nature of the magnetic field that compresses the solar wind plasma and forms jets upon crossing the bow shock. Although most jet generation mechanisms focus on processes at the quasi-parallel bow shock, jets are also observed downstream of the quasi-perpendicular shock. Proposed sources for these jets include magnetic flux tubes connecting to the quasi-parallel shock, mirror mode waves, non-reconnecting current sheets, reconnection outflows, gyrating ion populations or

---

★ E-mail: eva.kramer@umu.se

ripples at the quasi-perpendicular bow shock (Kajdič et al. 2021; Vuorinen et al. 2023; Raptis et al. 2020b). Despite the various proposed mechanisms for jet formation, the dominant mechanisms have yet to be identified.

After their generation at the bow shock, jets propagate through the magnetosheath toward the magnetopause. During this transit, jets often lose their identity by slowing down so they no longer meet the jet criteria, and only a subset reach the magnetopause (LaMoury et al. 2021; Krämer et al. 2025a). Although, under radial IMF conditions jets still frequently impact the magnetopause (Plaschke et al. 2016, 2020). When a jet reaches the magnetopause, it can be geoeffective in several ways: for example by triggering localized, bursty reconnection (Hietala et al. 2018; Ng et al. 2021) and causing transient displacement of the boundary (e.g. Amata et al. 2011; Shue et al. 2009; Hietala et al. 2012; Escoubet et al. 2020; Ma et al. 2024; Archer et al. 2012).

While most studies have focused on local compression effects, Shue et al. (2009), Němeček et al. (2023), and Kim et al. (2025) reported a local compression of the magnetopause as well as a sunward motion of the magnetopause. The impact area reported by Shue et al. (2009) was about 1 $\mathrm{R_E}$ deep and 2 $\mathrm{R_E}$ wide. The authors suggested that rebound after the initial impact point should propagate away as a surface wave, however, the spacecraft constellation did not allow this to be studied. Němeček et al. (2023) pointed out the the inward magnetopause displacement was about $1-2\,\mathrm{R_E}$, while the outward displacement was larger, up to 4 $\mathrm{R_E}$. Ma et al. (2024) suggested a simpler interaction of jets with the magnetopause: an isolated jet causes an indentation-rebounce-relaxation sequence at the magnetopause with spatial scales up to 3.2 $\mathrm{R_E}$ and temporal scales between 0.9−4.7 min. Using a 2.5D hybrid-kinetic simulation, Omidi et al. (2016) suggested that pressure variations in the magnetosheath caused by magnetosheath jets and cavities cause continuous magnetopause movement.

Following local magnetopause deformations, jets can also excite compressional waves that couple to field-aligned Alfvén waves, which are detectable by ground-based magnetometers (Archer et al. 2013; Norenius et al. 2021; Wang et al. 2022; Krämer et al. 2025). As a result of jet-triggered ULF waves, brightening of discrete dayside aurora has been associated with jets (Wang et al. 2018; Qiu et al. 2024). In addition, an isolated jet has been shown to trigger the magnetopause surface eigenmode, a standing surface wave on the magnetopause (Archer et al. 2019). In this specific event, the standing surface wave was confined to the subsolar region between 9 – 15 h magnetic local time. Further toward the flanks, the wave traveled tailward and acted as a seed for the Kelvin-Helmholtz instability (Archer et al. 2021).

Jet–magnetopause interactions can transfer energy and momentum from the solar wind into the magnetosphere. The fundamental question is: How do these interconnected, dynamic jets interact with the magnetopause? Addressing this question is challenging using spacecraft data alone, which are inherently limited in spatial coverage. To overcome this limitation, we employ a global, three-dimensional hybrid-kinetic simulation to investigate the spatial and temporal interaction between magnetosheath jets and the magnetopause. We therefore investigate how these interconnected jets interact with the magnetopause and the temporal evolution of such a jet-magnetopause interaction.

2 METHODS

In this section we first introduce the simulation, Amitis (Fatemi et al. 2017), and then explain how we identify jets and the magnetopause.

2.1 Simulation

We use the hybrid-kinetic plasma code Amitis (Fatemi et al. 2017) to model the interaction between the solar wind and Earth's magnetic field. In this model, ions are represented by macro-particles and electrons as a massless, charge-neutralizing fluid. We briefly describe the main features of the model here but we refer the reader to Fatemi et al. (2017) for a more detailed description of the model. We use the upgraded version of Amitis which runs on multiple GPUs (Fatemi et al. 2022), and in addition to other planetary bodies (`https://amitiscode.com/Publications.html`), it has recently been successfully applied to the Earth's plasma environment (Fatemi et al. 2024).

The simulation uses Cartesian cubes of length 500 km as grid cells. We use the following coordinate system to present our results: $+x$ points towards the Sun, $+z$ is anti-parallel to the magnetic dipole, and the y-axis completes the right hand coordinates system. The magnetic dipole has a strength of $31.78\,\mu\mathrm{T}\cdot\mathrm{R_E}^3$, where $\mathrm{R_E}$=6371 km is the Earth radius. The inner boundary of the simulation domain is a sphere with radius 30000 km (≈4.7 $\mathrm{R_E}$). No scaling is applied in our model, and the solar wind interaction with Earth takes place at its realistic, physical scales (Fatemi et al. 2024).

In this study we used two simulation runs, one with an sunward IMF ($\mathbf{B}_{\mathrm{IMF}} = [4.8, -1.3, 0.0]$ nT, denoted as run RX hereafter) and one with a westward IMF ($\mathbf{B}_{\mathrm{IMF}} = [0.0, +5.0, 0.0]$ nT, denoted as run RY hereafter). The RX run has previously been used in the analysis by Fatemi et al. (2024, denoted R1Y) and Krämer et al. (2025a, denoted RX). The remaining parameters are the same with a solar wind velocity $\mathbf{v}_{\mathrm{sw}} = [-400, 0, 0]$ km/s, a solar wind density $n_{\mathrm{sw}} = 7\,\mathrm{cm}^{-3}$, and a solar wind temperature $k_B T_{\mathrm{sw}} = 10$ eV. With only hydrogen ions being modeled, the resulting dynamic pressure in the solar wind $P_{\mathrm{sw}} = n_i m_i v_i^2 = 1.86$ nPa. The simulation data on each run is stored every 4 s. In the RX run, we inject 15 macroparticles per cell at the inflow boundary, and 17 macroparticles in the RY run. Even though the grid resolution is larger than the proton inertial length in the solar wind $\delta_i = 86$ km, Tóth et al. (2017) showed that as long as the global scales of a simulation are larger than δ_i, the model is not sensitive to δ_i. We refer the reader to section 2.5 in Fatemi et al. (2024) for a more detailed discussion of the simulations limitations.

2.2 Magnetopause identification

Studying the interaction of magnetosheath jets with the magnetopause requires identification criteria for those structures. We start by explaining how we identified the magnetopause which relies on changes in the magnetic field along the z axis, B_z. The modeled magnetic field in Amitis consists of two components; a static dipole magnetic field that represents Earth's magnetic field and a variable magnetic field from the hybrid plasma solver which represents deviations from the dipole magnetic field. In the dayside magnetosphere, the Earth's dipole magnetic field is enhanced due to current flowing on the magnetopause such that B_z from the solver enhances the magnetic field on the dayside. Outside the magnetosphere, in the solar wind and magnetosheath, the Earth's dipole magnetic field does not contribute and therefore the solver needs to counteract the contribution from the static dipole magnetic field. Since the magnetopause marks the boundary between the solar wind and the magnetosphere,

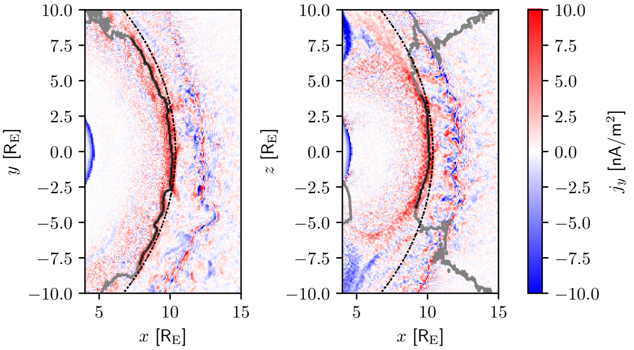

Figure 1. The current j_y in the xy plane (right) and xz plane (left) at simulation time 640 seconds (10:40). The gray represents the contour line where the solver B_z changes sign. The black solid line represents the identified magnetopause where $|y| < 8\,\mathrm{R_E}$ and $|z| < 4\,\mathrm{R_E}$ and $x > 5\,\mathrm{R_E}$. The black, dashed line represents the magnetopause model by Chao et al. (2002) (same as presented by Fatemi et al. (2024)).

one expects the solver B_z to change sign across the magnetopause (i.e., the magnetopause current). One can therefore identify the magnetopause by identifying places where the solver B_z changes sign. This change in B_z also indicates that there is a current flowing, the magnetopause current. We illustrated this boundary in Figure 1 showing the current density component j_y, calculated from Ampère's law, and the identified contour for the solver B_z (gray line). This criteria should only be used in the subsolar magnetosheath, and therefore we restrict ourselves to $|y| < 8\,\mathrm{R_E}$ and $|z| < 4\,\mathrm{R_E}$ and $x > 5\,\mathrm{R_E}$ (black, solid line). Outside this area, the contour where B_z changes sign, does not represent the magnetopause anymore, due to, for example, the cusp region. See for example gray line in Figure 1 where $|z| > 4\,\mathrm{R_E}$. We also require the identified magnetopause to be a single connected surface.

In order to quantify the displacement of the magnetopause from its ideal shape, we fitted a paraboloid of form $x = ay^2 + bz^2 + c$ to the identified magnetopause for every available time step with a, b, c being fitting parameters and x, y, z the coordinates (in units of R$_\mathrm{E}$) of simulation cells identified as the magnetopause. We then took the average of the fitting parameters a, b, c for all time steps and consider this averaged paraboloid as the average magnetopause location, where c also represents the stand-off distance of the magnetopause. We refer to the average magnetopause location as the nominal magnetopause. For RX(RY), we found $\langle a \rangle = -0.047 \pm 0.004$ ($\langle a \rangle = -0.0491 \pm 0.0006$), $\langle b \rangle = -0.057 \pm 0.005$ ($\langle b \rangle = -0.062 \pm 0.002$), and $\langle c \rangle = 10.15 \pm 0.08$ ($\langle c \rangle = 9.98 \pm 0.01$). The presented uncertainty is the standard deviation of the average magnetopause location. In comparison, empirical models, for example by Chao et al. (2002) predicts a functional form with a stand-off distance $10.5\,\mathrm{R_E}$ for the the solar wind conditions applied in our simulations, which is comparable to the stand-off distance obtained from our model (i.e., $10.2\,\mathrm{R_E}$ and $9.98\,\mathrm{R_E}$ for the RX and RY simulations respectively).

2.3 Jet identification

To identify jets we use a similar method to the criterion proposed by Plaschke et al. (2013) identifying jets as dynamic pressure enhancements in the magnetosheath where the dynamic pressure in the magnetosheath calculated only from v_x exceeds half of the upstream dynamic pressure: $P_{\mathrm{dyn,x}} > 0.5\,P_{\mathrm{dyn,sw}}$. This criterion should only be applied in the subsolar magnetosheath in the region where the solar zenith angle is below 30°. In regions where the solar zenith angle exceeds 30° we require that $P_{\mathrm{dyn,x}} > P_{\mathrm{dyn,sw}}$. This step-wise change of the criteria will likely introduce artifacts in the jet structure where the solar zenith angle is 30°. While Plaschke et al. (2013) additionally required a v_x enhancement in time intervals 1 minute prior and after the jet observation, we did not use such a criterion.

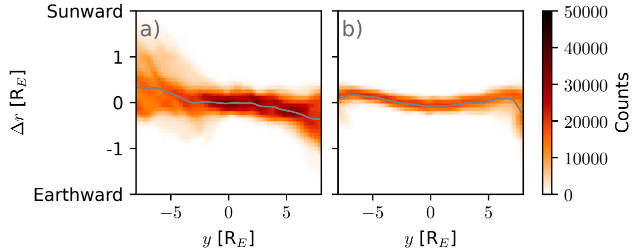

Figure 2. The magnetopause displacement for the RX run (a) and RY run (b). For each simulation cell identified as the magnetopause we calculated the distance to the nominal magnetopause. The gray line represents the median value for each y-bin.

3 RESULTS

3.1 Geometry of the magnetopause

We begin by quantifying how far the identified magnetopause deviates from the nominal magnetopause in both simulations. To do this, we calculated the smallest distance between each simulation cell associated with the identified magnetopause to the nominal magnetopause. These results are presented in Figure 2, with Figure 2a showing the results for the RX run and Figure 2b for the RY run. The gray line in each panel indicates the median displacement within each bin along the y-axis. The RX run exhibits a higher overall count rate (i.e. number of cells that are identified as the magnetopause) than the RY run, due to its longer physical simulation time. Overall, the magnetopause is more displaced in the RX run than in the RY run which is due to the parallel shock and foreshock forming upstream in the RX run, as discussed further below.

In the RX run (Figure 2a), an asymmetry emerges between the dawn ($y < 0$) and dusk side ($y > 0$). On the dawn side, the magnetopause is predominantly displaced sunward ($\Delta r > 0$), while on the dusk side, it is mainly displaced earthward ($\Delta r < 0$). Since the median deviation from the nominal magnetopause reaches about $0.3\,\mathrm{R_E}$ on the dawn side, the nominal magnetopause is not a good representation of the average magnetopause location and the median is a better measure. This expansion of the magnetopause occurs commonly under radial IMF conditions downstream of the quasi-parallel bow shock (Suvorova et al. 2010) and causes the magnetopause to be asymmetric under almost radial IMF. This highlights that even the IMF B_x component controls the shape of the magnetopause and a simple rotational symmetric form for the magnetopause (Chao et al. 2002; Shue et al. 1997) is not sufficient when IMF B_x is large relative to the other components. As a result, our nominal magnetopause underestimates the stand-off distance of the nominal magnetopause downstream of the quasi-parallel bow shock.

The RY run (Figure 2b) shows a more symmetric displacement between dawn and dusk. Notably, for regions where $|y| > 5\,\mathrm{R_E}$, the magnetopause tends to shift sunward. This shift suggests that the assumed paraboloid shape used to define the nominal magnetopause may not capture the actual structure of the magnetopause. However, these deviations are relatively minor. For the region where $|y| > 7\,\mathrm{R_E}$, the magnetopause starts to strongly deviate earthward, which is more pronounced on the dusk side compared to the dawn side. This stronger earthward shift is an artifact from our magnetopause identification method and the maximum extent of the selection criteria along y should have been more restricted.

3.2 Jet interaction with the magnetopause

These observed deformations in the RX run raise the question of what mechanisms are responsible for driving such magnetopause dynamics. While large-scale solar wind transients (such as interplanetary coronal mass ejections or co-rotating interaction regions) are known to cause significant distortions, our simulation setup explicitly excludes these events. Since the magnetopause is a pressure balance boundary, ultimately, a pressure imbalance is needed to deform the magnetopause. In our simulation set-up the magnetic pressure in the magnetosphere is constant, leaving pressure variations in the magnetosheath as the cause of magnetopause deformation. We can therefore study the effects of foreshock related processes, and specifically focus on magnetosheath jets, since they are known to cause a pressure imbalance at the magnetopause deforming the magnetopause locally (Amata et al. 2011; Shue et al. 2009; Hietala et al. 2012; Escoubet et al. 2020; Ma et al. 2024; Archer et al. 2012). We therefore continue our analysis by focusing on the jet–magnetopause interactions in the RX simulation (in the RY run we could not identify any jets close to the magnetopause and that serves as a basis for our analysis and comparison with the results obtained from the RX run).

Figure 3 presents snapshots of the magnetopause and nearby magnetosheath jets (gray structures) at selected times: 11:20, 11:40, 12:00, 12:20, 12:40, 13:00, 14:00, and 15:00. This development is also shown in Movie S1 that can be found in the Supplementary Material. To focus on interactions, we visualize only those jets located within 8000 km of the identified magnetopause. This constraint limits our ability to estimate the full jet size, as only the portion near the magnetopause is shown. Figure 3 might therefore suggest that jets are rather isolated structures and not interconnected as suggested by Fatemi et al. (2024). However, we are using the same simulation run as Fatemi et al. (2024) (simulation run R1Y in Fatemi et al. (2024)) which indeed shows interconnected structure of jets and the seemingly isolated structure is an effect of our restriction to jets close the magnetopause. The magnetopause is color-coded by its displacement from the nominal position: blue indicates an earthward shift (negative distance), while red indicates a sunward shift (positive distance). The displacement indicates that the magnetopause is not a smooth boundary in our simulation but is deformed and its form is changing over time.

In Figure 3, jets are observed near the magnetopause on both the dawn and dusk sides, but their structures differ significantly close to the boundary. On the duskside, jets exhibit an elongated shape along the y-direction, whereas dawnside jets appear more patchy and tend to extend along z. These jets occur downstream of the quasi-parallel bow shock, where $\theta_{\mathrm{Bn}} < 45°$ in the subsolar region, regardless of whether they are located on the dawn or dusk side, due to the nearly radial IMF. The apparent spherical cutoff of jets in Figure 3 toward the flanks results from a sudden increase in the dynamic pressure threshold at a solar zenith angle of 30° and does not represent a physical boundary.

Jet formation is often associated with the foreshock region containing ultra-low frequency (ULF) waves (Karlsson et al. 2021), generated by backstreaming ions reflected from the bow shock (Gary 1991). In our observations, such wave-like magnetic field fluctuations upstream of the bow shock (Eastwood et al. 2005; Wilson III 2016) occur approximately where $y \lesssim 4\,\mathrm{R_E}$ (though this boundary varies over time; see Movie S2 in the Supplementary Material). We therefore identify this region as the ULF wave foreshock.

To illustrate jet dynamics, we focus on the example jet marked by a purple arrow in Figure 3. At 11:20 (Figure 3a), the jet is located near $y \approx 0$, and the identified magnetopause closely aligns with its nominal position. By 11:40 (Figure 3b), the jet induces a local indentation in the magnetopause. Dawnward of the jet, a sunward protrusion begins to develop, forming a red bulge to the left of the jet. At 12:00 (Figure 3c), this protrusion intensifies and becomes elongated along the z-axis, exceeding its extent in y. As time progresses, the jet continues to push the magnetopause inward, amplifying both the earthward indentation and the sunward bulge. These features propagate toward the $-y$ flank (Figure 3d–h). By 13:00, the sunward protrusion spans at least from $-4\,\mathrm{R_E}$ to $4\,\mathrm{R_E}$, while the earthward indentation remains confined between $-4\,\mathrm{R_E}$ and $+2\,\mathrm{R_E}$ in the z direction. At 14:00 and 15:00, the protrusion intensifies further, even though the visible portion of the jet near the magnetopause diminishes (Figure 3h).

This sequence highlights not only the dynamic evolution of jet morphology but also the persistence of this particular jet over more than three minutes as it moves toward the flank. By 15:00, the sunward protrusion extends beyond the field of view, where the magnetopause can no longer be identified using our method.

3.3 Virtual observers in the magnetosheath and magnetosphere

To estimate the propagation speed of the magnetopause disturbance, we placed virtual observers in the $z = -1.5\,R_E$ plane, offset by $-0.5\,R_E$ in the $\hat{x}$ direction from the nominal magnetopause (Figure 4a). Each column in the figure corresponds to a virtual observer, while the rows show (top to bottom) plasma density n, velocity $\mathbf{v}$, magnetic field $\mathbf{B}$, and dynamic pressure calculated using v_x ($P_{\mathrm{d,x}}$). In the absence of deformations, the observers are expected to remain inside the magnetosphere, where the magnetic field is relatively stable and plasma density and velocity are low. When an earthward indentation propagates past an observer, the plasma properties become magnetosheath-like: magnetic field strength decreases, while density, velocity, and dynamic pressure increase. Such indentations are visible in the magnetic field (third row) which show a decrease in B_z at each observer location, indicating earthward indentation of varying intensity. As shown in Figure 3, these disturbances originate near the subsolar point and propagate toward the flanks. We therefore track the motion using the local minimum in B_z associated with the initial magnetopause movement, marked by vertical dashed lines in Figure 4a. The estimated propagation speeds are 133 km/s between observers 1 and 2, 176 km/s between observers 2 and 3, and 182 km/s between observers 3 and 4, suggesting that the disturbance accelerates over time. The propagation direction lies along the magnetopause boundary, primarily in the $-y$ and $-x$ directions, with the y-component dominating closer to the subsolar point.

In addition to the B_z decrease, increases in P_{dyn} and n are observed, consistent with the virtual spacecraft observing magnetosheath plasma. The first observer at [9.5, -1.5, -1.5] $\mathrm{R_E}$ (first column in Figure 4a) records the weakest disturbance, likely because the magnetopause indentation was still developing and had a relatively small amplitude. Subsequent observers detect a velocity component v_x that initially becomes negative (earthward motion) and then turns positive (sunward motion), supporting the interpretation that the magnetopause is first displaced earthward and then rebounds

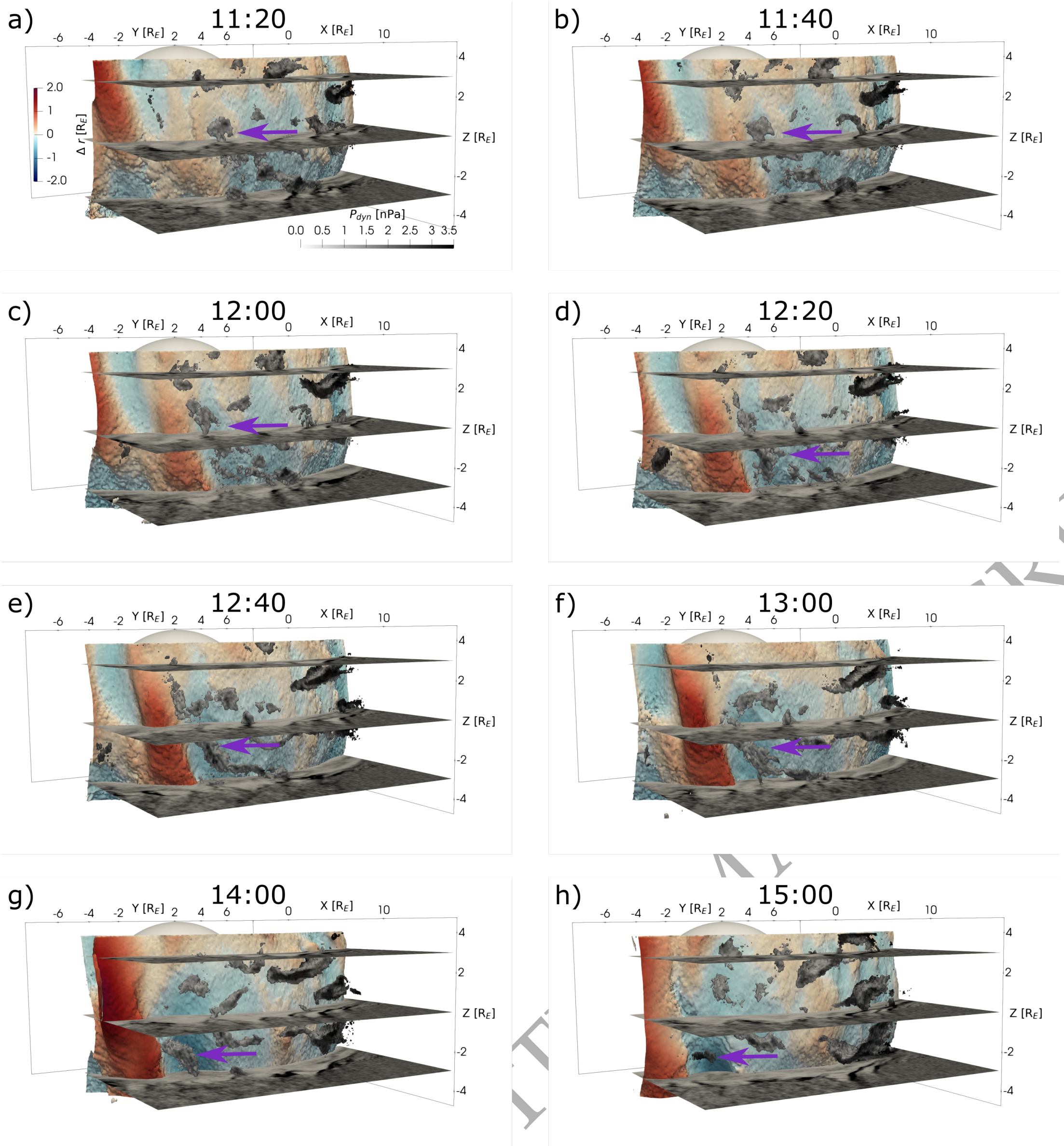

Figure 3. The interaction of jets with the magnetopause at 11:20, 11:40, 12:00, 12:20, 12:40, 13:00, 14:00, and 15:00 in the RX simulation. The surface represents the magnetopause and the coloring marks the distance to the ideal magnetopause. The gray structures are magnetosheath jets that are located within 8000 km of the magnetopause. The three planes, parallel to the xy plane, are located at $z = \{-3, 0, 3\}$ R$_\mathrm{E}$. The sphere located behind the magnetopause is the conducting boundary with a radius of 4.7 R$_\mathrm{E}$. The purple arrow follows one jet evolving over time.

sunward. This effect in v_x intensifies toward the flank. The first two observers (first and second column in Figure 4a) also detect a second magnetic field disturbance associated with a dynamic pressure increase near the end of the RX simulation, which also seems to be moving from observer 1 to observer 2.

We also placed virtual observers in the magnetosheath, offset by +0.75, R_E in the $\hat{x}$ direction from the nominal magnetopause (Figure 4b). In the bottom row, jets are identified where $P_{\mathrm{d,x}}$ exceeds the threshold $P_{\mathrm{sw}}/2$ (orange line). Jets observed (last row in Figure 4b) just prior to the magnetopause deformation (vertical dashed line) are those associated with the disturbance. These jets exhibit a strong negative v_x component, consistent with their movement toward the magnetopause and a positive v_y component (second row) in spite of the jet's apparent motion toward $-y$ as seen in Figure 3. The time lag (about 30 – 60 s) between jet detection and magnetopause response reflects the time required for the disturbance caused by the jet to travel the 1.25 R$_\mathrm{E}$ to the magnetospheric observers. Just before the jet detection, all observers except the first one, show an increase in B_z (third row), corresponding to the sunward bulges of the magnetopause seen in Figure 3.

3.4 The connection between foreshock structures and jets

An interesting observation in our simulation is that neither the velocity of the magnetopause surface wave nor the apparent motion of the jets match the ion bulk velocity in the jet. The magnetopause surface wave primarily moves in the $-y$ direction and the jet appears to follow in this direction. However, the bulk velocity of the ions in the jet (observed approximately at +0.75 R$_\mathrm{E}$ $\hat{x}$ from the magnetopause), is mainly directed along $-x$. This discrepancy suggests that the jet's

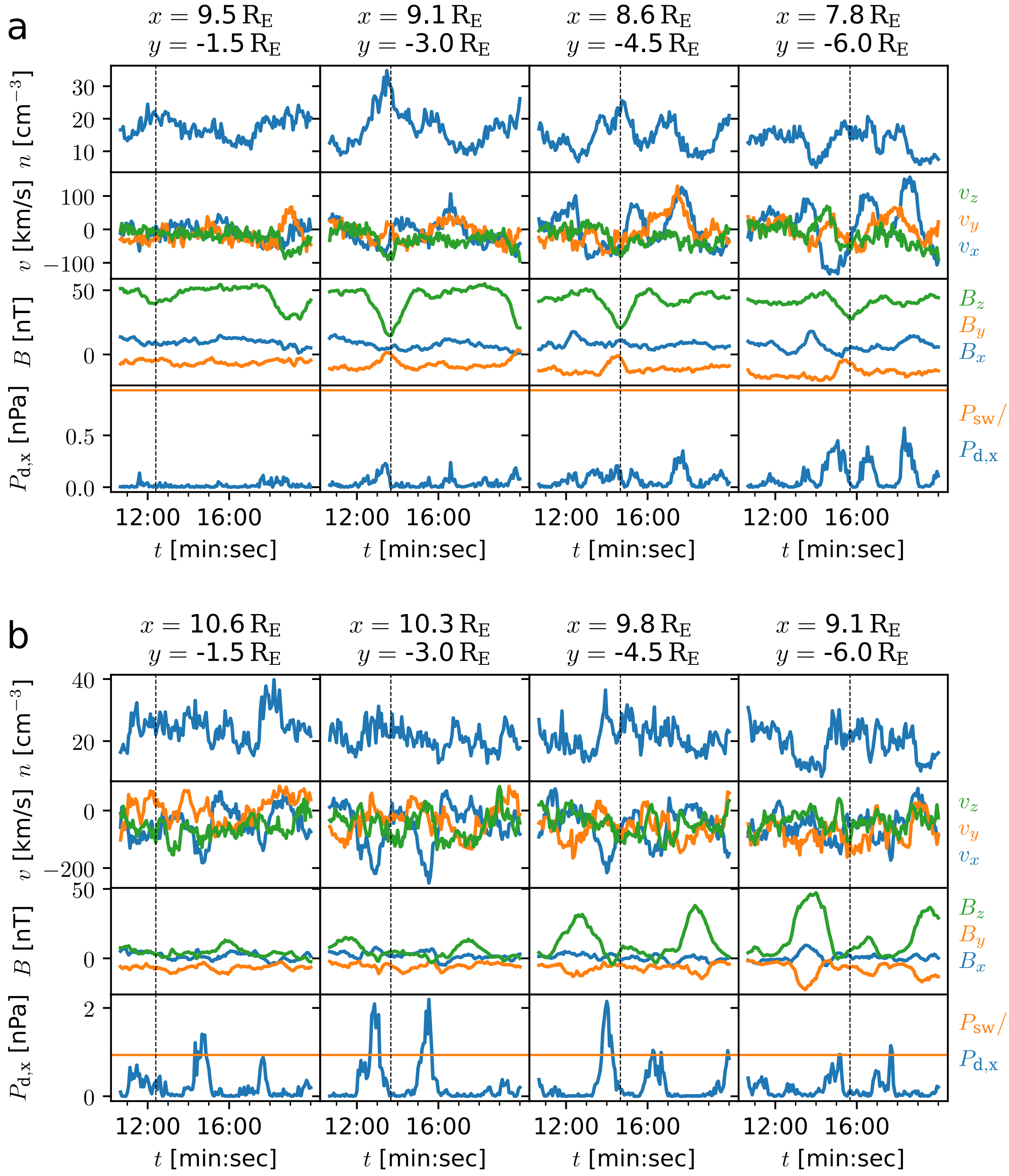

Figure 4. a: Virtual observers in the $z = -1.5\,R_E$ plane, offset by $-0.5\,R_E$ in the $\hat{x}$ direction from the nominal magnetopause with equal spacing along y. The exact x, y position is specified above each column. The first row shows the density $\boldsymbol{n}$, the second row the velocity $\boldsymbol{v}$, the third row the magnetic field $\boldsymbol{B}$, and the fourth row the dynamic pressure calculated with v_x only P_{dyn}. The vertical dashed lines give the time of the local minimum of B_z associated with the passing of the magnetopause indentation highlighted in Figure 3. b: Same as a but with virtual observers offset by $+0.75\,R_E$ in the $\hat{x}$ direction from the nominal magnetopause such that all observers are located in the magnetosheath.

bulk velocity alone cannot explain its apparent motion in Figure 3. A similar phenomenon has been reported using spacecraft observations where a magnetic field structure associated with the jet moved slower than the jet itself (Raptis et al. 2022b). One possible explanation for our observations is continuous jet formation at the bow shock: if the jet source moves along the bow shock while continuously generating a jet, it could create the apparent motion in the $-y$ direction, even though the bulk flow is directed along $-x$.

Jet formation has been linked to foreshock processes, in particular magnetic field pertubations enhancements in the foreshock, called foreshock compressive structures (Suni et al. 2021, 2023). We therefore examined the relative magnetic field enhancement in the $z = -1.5\,\mathrm{R_E}$ plane at different times and their relation to jets (black contours), shown in Figure 5. The Figure shows further that jets are frequently accompanied by magnetic field enhancements (red), particularly for jets located near the bow shock. We marked the jet that causes the magnetopause surface wave described in Figure 3 with purple arrows. The magnetopause is the magenta line and is deformed upon jet impact. Close to the bow shock these marked jets are associated with increases in the magnetic field strength and therefore likely connected to foreshock compressive structures. This is also closely related to the "magnetokinetic" formation mechanism proposed by Omelchenko et al. (2021). The authors suggest that the compression and penetration of solar wind plasma is driven by magnetic perturbations due to turbulence that subsequently cause the formation of jets. Our observed enhancements in the magnetic field are also a magnetic perturbation.

In the foreshock region, we observe compressional waves that can be identified as fast-mode waves as the density and magnetic field enhancements are in phase (data not shown). These fast mode waves, potentially classifiable as foreshock compressive structures if their magnetic field enhancements are sufficiently strong, exhibit a stripe-like pattern in the foreshock, see the gray, dashed lines in Figure 5. These stripe-like wavefronts are convected with the solar wind toward the bow shock. One possible explanation for the apparent jet motion along the $-y$ direction is that these waves, as they propagate toward the bow shock, continuously generate jets. Since the stripe-like wavefronts are not aligned with the solar wind flow, the jet formation site moves along the wavefront, and therefore results in an apparent jet movement along $-y$, even though the ion bulk velocity is directed along $-x$. The movement of these stripe-like foreshock waves towards the bow shock is also shown in Movie S3 in the Supplementary Material. While our results are consistent with the findings of Suni et al. (2021), who reported that jets are often associated with magnetic field enhancements, the form of the upstream waves in our simulation differs from those described in their study. The reason for this discrepancy remains unclear, but it may be due to differences in simulation setup. For example, Suni et al. (2021) use a 2D spatial domain, different IMF cone angles, or the fact that they use a hybrid-Vlasov simulation while we use a hybrid-PIC simulation. Consequently, their setup does not produce continuous jet formation at the bow shock.

We suggest that the foreshock waves cause an apparent jet motion in another direction than the bulk flow inside the jet which subsequently drive the magnetopause surface wave tailward. This apparent jet motion has yet to be observed with spacecraft observations. Detecting such events observationally is challenging and requires a fortunate combination of spacecraft positioning and solar wind conditions. Specifically, spacecraft must be located near the magnetopause, with separations of approximately 1 R_E in the y-direction and minimal separation in x and z. Even under these ideal conditions, tracking a jet remains difficult due to its rapidly evolving properties. We found one potential event that fits into our described mechanism for jet generation, that we briefly present in Appendix A.

3.5 Kelvin-Helmholtz instability on the dusk magnetopause

So far we have focused on the dawn side of the magnetopause which is located downstream of the ULF wave foreshock and is subject to direct jet impact causing large scale magnetopause deformations. But jets are even present on the dusk side where they appear (close to the magnetopause) as elongated structures aligning with the magnetopause with high dynamic pressure (Figure 3 where $y > 0$). These jets downstream of the quasi-perpendicular-like bow shock are magnetically connected to the quasi-parallel bow shock (see orange stream lines in Figure 6e). We therefore suggest that those jets represent flux tubes magnetically connected to the ULF foreshock (Kajdič et al. 2021). The magnetopause displacement on the dusk side is mainly earthward from its nominal position (see Figure 2), however, it appears that it is not direct jet impacts causing these earthward displacements. Instead, the current density (Figure 6c) reveals the position of the magnetopause which is not continuous but appears to be rippled including vortex-like structures. A similar structure of a rippled magnetopause can be seen in Figure 6a showing the magnetic field strength and in the particle density (Figure 6b). The vortices at the magnetopause indicate the formation of Kelvin-Helmholtz vortices at the dusk side magnetopause which is known to develop at magnetospheric boundary layers (for a review see Johnson et al. 2014). The time evolution of these vortices can be seen in Movie S2 in the Supplementary Material.

The Kelvin-Helmholtz instability (KHI) is mostly controlled by the velocity shear across the boundary (in this case the magnetopause), but a magnetic field along the wave vector has a stabilizing effects due to the magnetic tension force (e.g. Chandrasekhar 1961). The bulk speed is shown in Figure 6d, which shows that the speed in the dusk magnetosheath close to the subsolar point ($y < 10\,R_E$) is enhanced compared to the dawn side. Hence the velocity shear is greater on the dusk magnetopause compared to the dawn magnetopause. The magnetic field, however, has a stabilizing effect on the dusk magnetopause caused by the draping pattern of the magnetic field as shown by purple field lines in Figure 6e. On the dawn magnetopause, the magnetic field does not align with the wave vector (assuming it lies in the xy-plane) so there is no stabilization due to the magnetic tension force. Similarly, the density gradient across is larger across the dusk magnetopause (see Figure 6b) compared to the dawn magnetopause. A larger density gradient also stabilizes the KHI (Amerstorfer et al. 2007). Nevertheless, Kelvin-Helmholtz vortices are observed on the duskside, indicating that the larger velocity shear dominates over the increased magnetic tension force and the density gradient. In summary, in our simulation, jets do not drive the dynamics of the duskside magnetopause but this is rather controlled by the Kelvin Helmholtz instability.

4 DISCUSSION

We used a 3D, hybrid-kinetic simulation to investigate the spatial and temporal interaction of magnetosheath jets with the magnetopause. Our results show that magnetosheath jets can cause significant deformations of the subsolar magnetopause during low cone angle solar wind conditions.

4.1 The effects of jets depending on the bow shock regime

We find that the interaction differs depending on whether jets are located on the dawn side, which is located downstream of the ULF foreshock, or dusk side which contains the ULF foreshock boundary and the bow shock becomes more quasi-perpendicular-like.

On the dawn side, located downstream of the ULF foreshock, jets interact with the magnetopause producing a combined earthward and sunward distortion of the boundary. This behavior is consistent with spacecraft observations reported by Shue et al. (2009). The resulting deformation can be interpreted as a magnetopause surface wave that propagates toward the tail. In our simulation, this wave is continuously reinforced by continuous jet impacts, which further amplify its amplitude, even though virtual observers show the typical transient nature of jets as observed in spacecraft data. We find

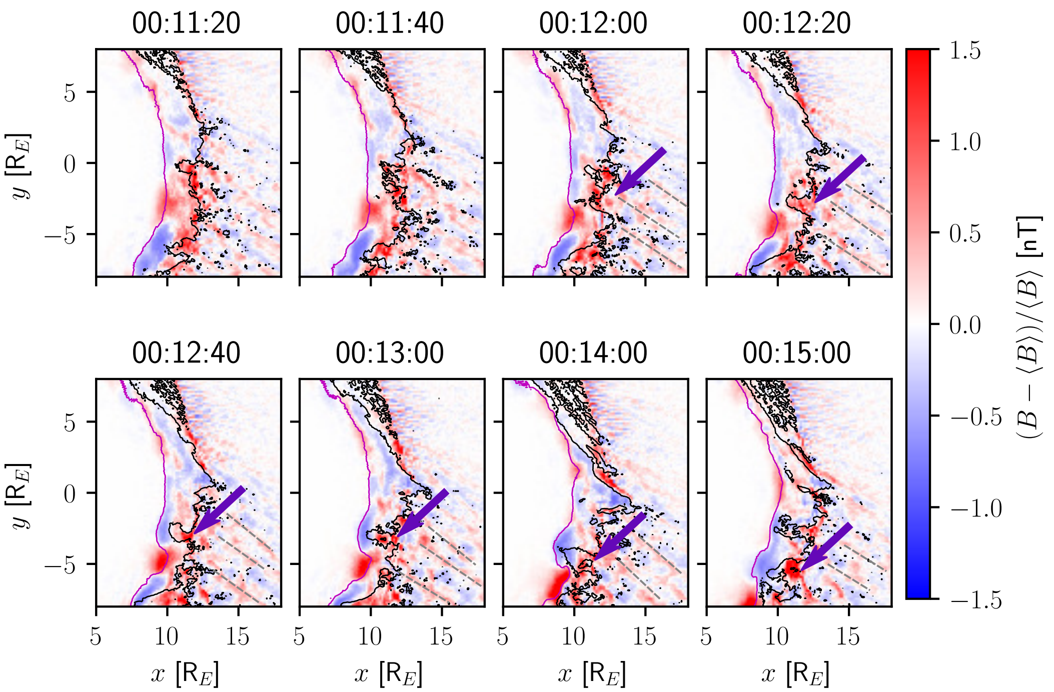

Figure 5. The relative magnetic field enhancement in the $z = -1.5\,\mathrm{R_E}$-plane at 11:20, 11:40, 12:00, 12:20, 12:40, 13:00, 14:00, and 15:00 [min:sec]. The magenta line represents the identified magnetopause and the black line the jet threshold. The purple arrows track the jet that causes the magnetopause surface wave described previously. The gray, dashed lines indicate the (highly dynamic) wave pattern in the foreshock.

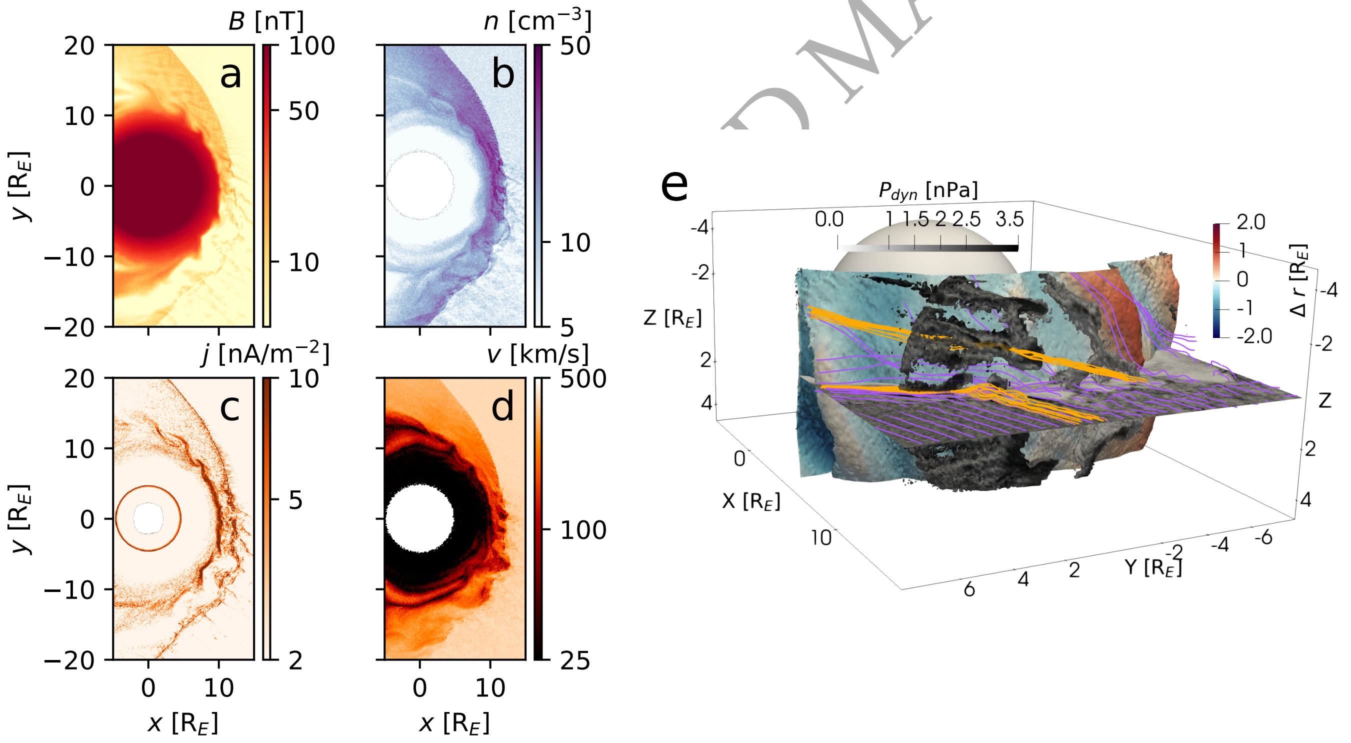

Figure 6. The magnetic field strength (a), particle density (b), current density (c), and the bulk speed (d) at 18:00. e: Draping of the magnetic field in the magnetosheath (purple field lines) and magnetic field lines connected to magnetosheath jets downstream of the quasi-perpendicular shock (orange). The $-z$-axis is pointing upwards for visualization purposes.

that the earthward displacement of the magnetopause does not exceed 1 $\mathrm{R_E}$, in agreement with the results of Wang et al. (2023). In contrast, the sunward displacement can reach up to 2 $\mathrm{R_E}$, indicating a stronger response in that direction. This matches observations where the sunward displacement of the magnetopause was larger than the earthward displacement (Němeček et al. 2023). However, due to the magnetopause expansion downstream of the quasi-parallel bow shock, our nominal magnetopause in that region is located earthward of average magnetopause location. The displacement might therefore actually be more symmetric, less than 1.5 $\mathrm{R_E}$ in both directions.

In the equatorial plane, the extent of the magnetopause disturbance remains relatively confined, whereas the deformation is more pronounced in the north–south direction. We suggest that this asymmetry arises from the influence of the magnetic tension force. Along magnetic field lines, roughly oriented in the north–south direction near the subsolar region, magnetic tension resists local deformation, causing the entire field line to bend instead. In contrast, in the east–west direction, where magnetic tension is negligible, the magnetopause can be more easily displaced. A similar asymmetry in magnetopause deformation upon jet impact has been observed in simulations of Mercury's magnetosphere (Guo et al. 2024) and Earth's magnetosphere (Chen et al. 2021) which has been attributed to the impact of foreshock turbulence. Similarly, Plaschke et al. (2009) suggested that the magnetopause in general, not only under jet impact, has a higher stability against field-aligned deformation.

On the dusk side, we do not observe the formation of a jet-driven magnetopause surface wave. Instead, Figure 2 reveals stronger earthward displacements caused by Kelvin Helmholtz instabilities (see Figure 6). Visual tracking of these vortices suggests that the instability is in its linear stage closer to the subsolar magnetosheath (see Movie S2 in the Supplementary Material), which likely explains the observed earthward magnetopause distortions. MHD simulations suggested that the Kelvin Helmholtz instability might occur more often in the dawn side flank due to the Parker spiral orientation of the IMF causing different plasma properties in the magnetosheath (Nykyri 2013). Similarly, observations suggested that KH waves preferably form on the dawn side under Parker spiral IMF orientation (Henry et al. 2017) and are larger at the dawnside compared to the duskside (Grimmich et al. 2025a). The RX simulation has a Parker Spiral-like IMF orientation where $B_x/B_y < 0$ (as opposed to the ortho-Parker spiral orientation where $B_x/B_y > 0$). Even though the cone angle is 15° and therefore lower than 45° as expected for the typical Parker Spiral, we expect a similar draping pattern for IMF as for a Parker Spiral IMF and therefore the KH instability to form at the dawn flank. However, the KH instability observed in the dusk flank and not in the dawn flank.

Even though the magnetic tension force would stabilize the magnetopause on the duskside, the greater velocity shear in our simulation causes Kelvin Helmholtz vortices to form at the dusk flank. Potentially, the non-stationary magnetopause, caused by jet impact (see Figure 2 and Movie S1), can act as a seed fluctuation for the Kelvin Helmholtz instability on the dusk side. However, it is not possible to test if the onset of the Kelvin Helmholtz instability would be delayed without jets since that would require changing the IMF in the simulation which also changes the draping pattern of the magnetic field in the magnetosheath. The question arises why we do not see Kelvin Helmholtz vortices in the RX run further tailward on the dawn flank where the velocity shear is larger. One possibility is that even though the boundary might be Kelvin Helmholtz unstable, magnetosheath jet interaction dominates the magnetopause dynamics. So even if a surface wave builds up in the linear stage, the continuous impact of magnetosheath jets disrupts the development of large Kelvin-Helmholtz vortices. In the RX simulation the foreshock might also be able to grow unusually strong due to the stable IMF direction which causes more jets to form and reach the magnetopause.

We use the RY run in order to compare with a situation without the quasi-parallel bow shock. Downstream of the quasi-perpendicular bow shock in the RY run with a 90° cone angle, the magnetopause moves little. In this simulation, jets are only observed close to the bow shock and they therefore do not impact the magnetopause (Krämer et al. 2025a). The stronger deviations from the nominal magnetopause for $y > |7|\,\mathrm{R_E}$ are caused by our magnetopause identification method not being suited for those distances from the Sun-Earth line for the RY run rather than any physical process. The absence of the dawn-dusk asymmetry in the RY run indicates that the asymmetry observed in the RX run is caused by the quasi-radial IMF and the associated foreshock.

4.2 Comparison to previous work

Before placing our results in the context of previous observations, it is important to emphasize that our simulation represents the limiting case of a steady solar wind, with a constant upstream solar wind. Under such conditions, the jets are linked to foreshock dynamics, whereas jets associated with solar wind discontinuities or transient structures do not form. Previous work shows that solar wind discontinuities can generate isolated, long-lived, and potentially more geoeffective jets (Suni et al. 2025), in contrast to the interconnected jets downstream of the quasi-parallel shock. Because low solar wind cone angles (< 30°) are rare, about 10% of the time (Vuorinen et al. 2023), only a subset of jets is produced under conditions comparable to our setup. This distinction is relevant when comparing to spacecraft observations, where the origin of individual jets is often ambiguous and different formation mechanisms may lead to a variability in their geoeffectiveness. Despite the absence of solar wind discontinuities, our results demonstrate that the foreshock alone is sufficient to generate jets capable of producing significant magnetopause perturbations, consistent with previous findings that foreshock activity can strongly modulate the magnetopause position (Grimmich et al. 2025b).

The majority of such studies have been based on spacecraft data and information on temporal development is therefore limited (e.g. Hietala et al. 2012; Escoubet et al. 2020; Ma et al. 2024; Amata et al. 2011; Archer et al. 2012). While Shue et al. (2009) reported both a combined earthward and sunward distortion, most studies focused on earthward movements (e.g. Hietala et al. 2012; Escoubet et al. 2020; Ma et al. 2024; Amata et al. 2011; Archer et al. 2012).

Our results suggests that several jets can impact the magnetopause at the same time in different locations similar to the observations by Escoubet et al. (2020). Furthermore, Ma et al. (2024) suggested a indentation-rebounce-relaxation sequence upon jet impact at the magnetopause with spatial and temporal scales of $0.5 - 3.2\,\mathrm{R_E}$ and $0.9 - 4.7$ min. While the temporal scales are similar, we could not observe a rebounce of the magnetopause that exceeds the nominal magnetopause after the initial indentation. However, due to the continuous impact and generation of jets at the magnetopause, caused by the interconnected nature of jets (Fatemi et al. 2024; Ren et al. 2024), we cannot isolate the response due to a single jet. Simulating a jet caused by a solar wind discontinuity might be able to reveal the impact upon an isolated jet. Since Ma et al. (2024) focused on isolated jets, the previously discussed differences might cause the interaction with the magnetopause to differ. Another study proposed that an isolated jet can trigger a magnetopause surface eigenmode, which are standing waves at the magnetopause (Archer et al. 2019). As our surface wave is moving towards the terminator, it is not a standing wave. One difference might be that an isolated jet, generated through a different mechanism, can trigger a magnetopause surface wave, but not foreshock generated jets.

5 CONCLUSION

We have investigated the spatial and temporal interaction of magnetosheath jets with the magnetopause using a 3D hybrid-kinetic simulation. Even though, virtual spacecraft observations show the typical transient nature of jets, 3D rendered figures indicate that jets can persist over longer times in the magnetosheath, likely due to continuous jet formation at the bow shock. We propose the following interaction scheme on the dawnside downstream of the ULF wave foreshock, for a low cone angle, Parker Spiral-like IMF:

- ULF waves in the foreshock region have $k_y < 0$ such that they propagate towards the dawn flank.
- The interaction between these waves and the bow shock leads to the formation of magnetosheath jets.
- In the magnetosheath these jets appear to move in the same direction as the foreshock waves while the bulk velocity of the ions in the jet is directed towards the magnetopause.
- These jets can subsequently cause magnetopause deformations. The magnetopause reacts asymmetrically upon jet impact. The magnetopause is more stable in the field-aligned direction than perpendicular to it due to the magnetic tension force.
- Due to the continuous interaction of the foreshock wave with the bow shock creating jets, the magnetopause surface wave is continuously reinforced, propagating toward the dawn flank and growing in amplitude.

On the duskside magnetopause, magnetosheath jets do not directly impact the magnetopause. However, through increased shear velocities at the magnetopause jets might contribute to the formation of Kelvin-Helmholtz vortices. For a low cone angle ortho-Parker Spiral-like IMF with $B_y > 0$, we would expect a similar interaction pattern on the duskside with duskward propagating waves and jets.

ACKNOWLEDGEMENTS

EK and MH were supported by Vetenskapsrådet grant 2018-03623 and the Swedish National Space Agency under grant 2022-00138. AP acknowledges the support by the Deutsches Zentrum für Luft- und Raumfahrt (DLR) under contract 50 OC 2201. The work of NG on this study was supported by DLR under contract 50 OC 2401. SF acknowledges financial support by the Swedish National Space Agency (Rymdstyrelsen), grant 2022-00183. The simulations were conducted on Vega Super Computer under EuroHPC Regular Access, grant EHPC-REG-2023R03-023. Work by HG was supported by the Swedish National Space Agency, grant 2023-00208.

We acknowledge NASA contract NAS5-02099 and V. Angelopoulos for use of data from the THEMIS Mission. Specifically: C. W. Carlson and J. P. McFadden for use of ESA data and O. LeContel and the late A. Roux for use of SCM data. The OMNI data were obtained from the GSFC/SPDF OMNIWeb interface at `https://omniweb.gsfc.nasa.gov`.

During the preparation of this work the authors used Microsoft Copilot in order to edit and rewrite the manuscript. After using this tool/service, the authors reviewed and edited the content as needed and take full responsibility for the content of the publication.

DATA AVAILABILITY

The simulation data used for this study is available at `https://doi.org/10.5281/zenodo.20732234` (Krämer et al. 2026).

REFERENCES

Amata E., Savin S., Ambrosino D., Bogdanova Y., Marcucci M., Romanov S., Skalsky A., 2011, Planetary and Space Science, 59, 482
Amerstorfer U., Erkaev N., Langmayr D., Biernat H., 2007, Planetary and Space Science, 55, 1811
Angelopoulos V., 2008, Space Science Reviews, 141, 5
Archer M., Horbury T., 2013, in Annales Geophysicae. pp 319–331
Archer M., Horbury T., Eastwood J., 2012, Journal of Geophysical Research: Space Physics, 117
Archer M., Horbury T. S., J. P. Eastwood Eastwood J., Weygand J. M., Yeoman T. K., 2013, Journal of Geophysical Research, 118, 5454
Archer M., Hietala H., Hartinger M. D., Plaschke F., Angelopoulos V., 2019, Nature Communications, 10, 615
Archer M., Hartinger M., Plaschke F., Southwood D., Rastaetter L., 2021, Nature communications, 12, 5697
Burch J., Moore T., Torbert R., Giles B.-h., 2016, Space Science Reviews, 199, 5
Chandrasekhar S., 1961, Hydrodynamic and Hydromagnetic Stability. Oxford University Press
Chao J., Wu D., Lin C.-H., Yang Y.-H., Wang X., Kessel M., Chen S., Lepping R., 2002, in COSPAR colloquia series. pp 127–135
Chen L.-J., Ng J., Omelchenko Y., Wang S., 2021, Geophysical Research Letters, 48, e2021GL093029
Eastwood J., Lucek E., Mazelle C., Meziane K., Narita Y., Pickett J., Treumann R., 2005, Space Science Reviews, 118, 41
Escoubet C., Fehringer M., Goldstein M., 2001, in Annales Geophysicae. pp 1197–1200
Escoubet C., et al., 2020, Frontiers in Astronomy and Space Sciences, 6, 78
Fatemi S., Poppe A. R., Delory G. T., Farrell W. M., 2017, in Journal of physics: Conference series. p. 012017
Fatemi S., Poppe A., Vorburger A., Lindkvist J., Hamrin M., 2022, Journal of Geophysical Research: Space Physics, 127, e2021JA029863
Fatemi S., Hamrin M., Krämer E., Gunell H., Nordin G., Karlsson T., Goncharov O., 2024, Monthly Notices of the Royal Astronomical Society, 531, 4692
Gary S. P., 1991, Space Science Reviews, 56, 373
Grimmich N., Plaschke F., Archer M., Heyner D., Mieth J., Nakamura R., Sibeck D., 2023, Database: THEMIS magnetopause crossings between 2007 and mid-2022, doi:10.17605/OSF.IO/B6KUX, `osf.io/b6kux`
Grimmich N., et al., 2024, Database: Cluster Magnetopause Crossings between 2001 and 2020, doi:10.17605/OSF.IO/PXCTG, `osf.io/pxctg`
Grimmich N., Settino A., Nykyri H. K., Archer M. O., Blasl K.-A., Pöppelwerth A., Nakamura R., Plaschke F., 2025a, Planetary and Space Science, p. 106182
Grimmich N., et al., 2025b, in Annales Geophysicae. pp 151–173
Guo J., et al., 2024, The Astrophysical Journal Letters, 978, L9
Henry Z. W., Nykyri K., Moore T. W., Dimmock A. P., Ma X., 2017, Journal of Geophysical Research: Space Physics, 122, 11
Hietala H., Plaschke F., 2013, Journal of Geophysical Research: Space Physics, 118, 7237
Hietala H., et al., 2012, in Annales Geophysicae. pp 33–48
Hietala H., Phan T. D., Angelopoulos V., Oieroset M., Archer M. O., Karlsson T., Plaschke F., 2018, Geophysical Research Letters, 45, 1732
Johnson J. R., Wing S., Delamere P. A., 2014, Space Science Reviews, 184, 1
Kajdič P., Raptis S., Blanco-Cano X., Karlsson T., 2021, Geophysical Research Letters, 48, e2021GL093173
Karlsson T., Brenning N., Nilsson H., Trotignon J. G., Valliéres X., Facsko G., 2012, Journal of Geophysical Research: Space Physics, 117, 1
Karlsson T., Raptis S., Trollvik H., Nilsson H., 2021, Journal of Geophysical Research: Space Physics, 126, e2021JA029269

Kim H., et al., 2025, Geophysical Research Letters, 52, e2025GL117683

Koller F., Plaschke F., Temmer M., Preisser L., Roberts O. W., Vörös Z., 2023, THEMIS Magnetosheath and Jet Intervals 2008-2021, `osf.io/s32yf`

Krämer E., Fatemi S., Hamrin M., Gunell H., Nordin G., 2025a, Geophysical Research Letters, 52, e2025GL115260

Krämer E., et al., 2025b, Space Science Reviews, 221, 1

Krämer E., Hamrin M., Gunell H., Baddeley L., Partamies N., Raptis S., Herlingshaw K., Schillings A., 2025, Journal of Geophysical Research: Space Physics, 130, e2025JA033792

Krämer E., Fatemi S., Gunell H., Hamrin M., Pöppelwerth A., Grimmich N., 2026, Data for "Magnetosheath Jet Interaction with the Magnetopause: Results from the 3D hybrid-kinetic Simulation Amitis" by Krämer et al., doi:10.5281/zenodo.20732234, `https://doi.org/10.5281/zenodo.20732234`

LaMoury A. T., Hietala H., Plaschke F., Vuorinen L., Eastwood J. P., 2021, Journal of Geophysical Research: Space Physics, 126, e2021JA029592

Ma J., et al., 2024, Geophysical Research Letters, 51, e2024GL111132

Ng J., Chen L.-J., Omelchenko Y. A., 2021, Physics of Plasmas, 28, 092902

Norenius L., et al., 2021, Journal of Geophysical Research: Space Physics, 126

Nykyri K., 2013, Journal of Geophysical Research: Space Physics, 118, 5068

Němeček Z., et al., 2023, Geophysical Research Letters, 50, e2023GL106131

Omelchenko Y. A., Chen L.-J., Ng J., 2021, Journal of Geophysical Research: Space Physics, 126, e2020JA029035

Omidi N., Berchem J., Sibeck D., Zhang H., 2016, Journal of Geophysical Research: Space Physics, 121, 3155

Papitashvili N. E., King J. H., 2020, "OMNI 1-min Data" [Data set], doi:https://doi.org/10.48322/45bb-8792

Plaschke F., et al., 2009, Journal of Geophysical Research: Space Physics, 114

Plaschke F., Hietala H., Angelopoulos V., 2013, in Annales Geophysicae. pp 1877–1889

Plaschke F., Hietala H., Angelopoulos V., Nakamura R., 2016, Journal of Geophysical Research, 121, 3240

Plaschke F., et al., 2018, Space Science Reviews, 214, 81

Plaschke F., Hietala H., Vörös Z., 2020, Journal of Geophysical Research: Space Physics, 125

Pöppelwerth A., et al., 2024, Database: Cluster - subsolar magnetosheath jet data 2000-2023 [Dataset], doi:10.17605/OSF.IO/XVDY6, `osf.io/xvdy6`

Qiu H.-X., Han D.-S., Shi R., Liu J., 2024, AGU Advances, 5, e2024AV001197

Raptis S., Karlsson T., Plaschke F., Kullen A., Lindqvist P.-A., 2020a, Magnetosheath Jets MMS (5/2015 - 6/2019) [Dataset], doi:10.5281/zenodo.3739553, `https://doi.org/10.5281/zenodo.3739553`

Raptis S., Karlsson T., Plaschke F., Kullen A., Lindqvist P., 2020b, Journal of Geophysical Research: Space Physics, 125, e2019JA027754

Raptis S., Karlsson T., Vaivads A., Pollock C., Plaschke F., Johlander A., Trollvik H., Lindqvist P.-A., 2022a, Nature Communications, 13, 598

Raptis S., Karlsson T., Vaivads A., Lindberg M., Johlander A., Trollvik H., 2022b, Geophysical Research Letters, 49, e2022GL100678

Ren J., Guo J., Lu Q., Lu S., Gao X., Ma J., Wang R., 2024, Geophysical Research Letters, 51, e2024GL109925

Shue J.-H., Chao J., Fu H., Russell C., Song P., Khurana K., Singer H., 1997, Journal of Geophysical Research: Space Physics, 102, 9497

Shue J.-H., Chao J.-K., Song P., McFadden J., Suvorova A., Angelopoulos V., Glassmeier K., Plaschke F., 2009, Geophysical Research Letters, 36

Sibeck D. G., Lopez R., Roelof E. C., 1991, Journal of Geophysical Research: Space Physics, 96, 5489

Suni J., et al., 2021, Geophysical Research Letters, 48, e2021GL095655

Suni J., et al., 2023, in Annales Geophysicae. pp 551–568

Suni J., Palmroth M., Turc L., Battarbee M., Pfau-Kempf Y., Ganse U., 2025, Journal of Geophysical Research: Space Physics, 130, e2025JA033995

Suvorova A., et al., 2010, Journal of Geophysical Research: Space Physics, 115

Toy-Edens V., 2024, 8 years of dayside Magnetospheric Multiscale (MMS) unsupervised clustering plasma regions classifications [Dataset], doi:10.5281/zenodo.10491878, `https://doi.org/10.5281/zenodo.10491878`

Tóth G., Chen Y., Gombosi T. I., Cassak P., Markidis S., Peng I. B., 2017, Journal of Geophysical Research: Space Physics, 122

Vuorinen L., Hietala H., Plaschke F., 2019, in Annales Geophysicae. pp 689–697

Vuorinen L., Hietala H., LaMoury A. T., Plaschke F., 2023, Journal of Geophysical Research: Space Physics, 128, e2023JA031494

Wang B., Nishimura Y., Hietala H., Lyons L., Angelopoulos V., Plaschke F., Ebihara Y., Weatherwax A., 2018, Journal of Geophysical Research: Space Physics, 123, 4879

Wang B., Nishimura Y., Hietala H., Angelopoulos V., 2022, Geophysical Research Letters, 49, e2022GL099768

Wang X., Lu J., Wang M., Zhou Y., Hao Y., 2023, Geophysical Research Letters, 50, e2023GL105270

Wilson III L. B., 2016, Low-frequency waves in space plasmas, pp 269–291

APPENDIX A: POSSIBLE SPACECRAFT EVENT

Our simulation raises the question of whether continuous jet generation, as observed in the model, can also be identified in spacecraft data. Using data from three THEMIS spacecraft, we examined one potential event, shown in Figure A1a presenting data between 2008-08-18 22:11 – 22:26 UT. The top panel displays magnetic field strength B, plasma density n, velocity v, and dynamic pressure $P_{\mathrm{d,x}}$ calculated using v_x only for THEMIS A, E, and D, ordered by their y-position. A jet was first observed by THEMIS A (highlighted in purple) at 22:18:58 UT, followed shortly by a jet detection at THEMIS E at 22:20:17 UT, located duskward of A. Subsequently, THEMIS D, positioned even further duskward, also recorded a jet at 22:21:01 UT, along with a sunward magnetopause motion (marked by a black, dotted line) around 22:18:45 UT. During the investigated time interval, the IMF and solar wind density and velocity, derived from the OMNI database (Papitashvili & King 2020), were relatively stable between 2008-08-18 22:04-22:33 UT as shown in Figure A1b. The large B_x component of the IMF compared to the B_y, B_z component indicates that the IMF cone angle was low. Both IMF $B_y, B_z > 0$ indicating that the quasi-parallel magnetosheath is expected to be located where $y > 0$ (opposite to the IMF orientation and location of the quasi-parallel magnetosheath in the presented simulation run).

The jet observation of THEMIS A (located closest to the subsolar point) and the magnetopause crossing observed by THEMIS E (located further tailward) almost coincide. This observation agrees with our proposed interaction scheme: flankward of the initial jet impact, an sunward distortion of the magnetopause. Although neither THEMIS A nor E crossed the magnetopause during this interval, the third row of Figure A1 shows that v_x was small or even positive prior to the jet observations, suggesting a possible sunward motion of the magnetopause. Due to the non-zero IMF B_z component, the jet would be expected to move both along the $+y$ and $+z$-direction. The jet is indeed observed first by Themis A, then E, and then D, indicating a movement in the $+y$ direction. However, we cannot determine the three-dimensional direction of motion from two spacecraft only nor did all spacecraft observe a definite magnetopause crossing, but only indications of the magnetopause moving prior to the jet observation. While this event indicates that a similar mechanism might be at play as in the simulation, a more careful analysis of spacecraft data is needed to fully confirm our hypothesized mechanism.

To find a potential observation, reinforcing our described interaction mechanism, we suggest combining databases with jet observations (Koller et al. 2023; Pöppelwerth et al. 2024; Raptis et al. 2020a) and databases with magnetopause crossing (Grimmich et al. 2023,

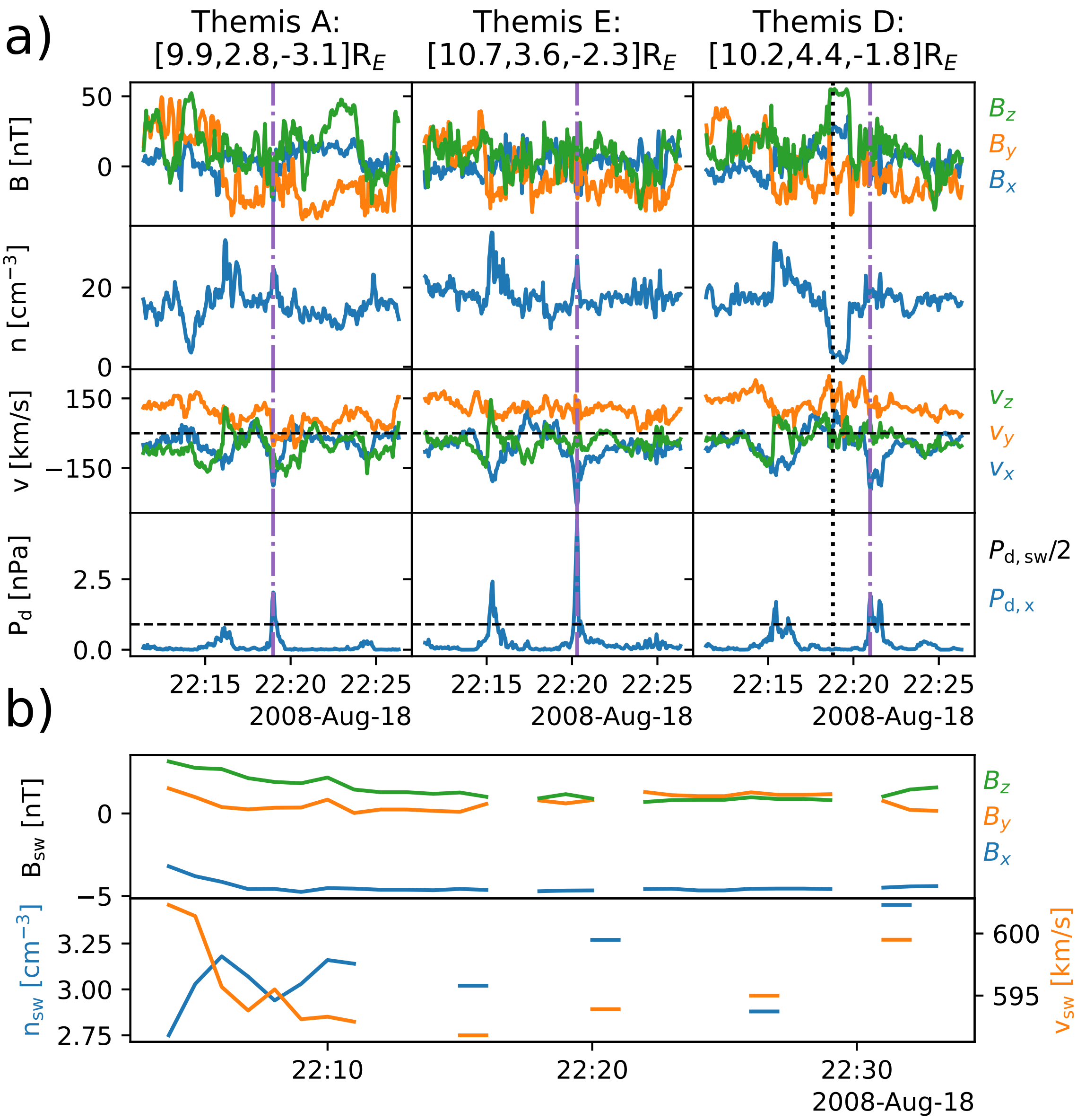

Figure A1. Event, possibly showing the apparent jet motion along y on 2008-08-18 22:11 – 22:26 UT. All data are given in GSM coordinates. A: $\boldsymbol{B}$, n, v, $P_{\rm dyn}$ (top to bottom) for the THEMIS A, E, D probes (left to right). The purple dashed-dotted line marks the dynamic pressure peak of a jet and the black dotted line the magnetopause crossing by THEMIS D. B: Solar wind parameters $\boldsymbol{B}$, n, and v (top to bottom).

2024; Toy-Edens 2024) from the THEMIS mission (Angelopoulos 2008), the MMS mission (Burch et al. 2016) and the Cluster mission (Escoubet et al. 2001) in the future. This would allow to find potential spacecraft conjunctions showing jet occurrence and associated magnetopause movements.

APPENDIX B: SUPPLEMENTARY MOVIES

Three movies are provided as supporting information to the main text and figures in this manuscript.

Movie S1.

Same layout as Figure 3 but as a movie to illustrate the time evolution.

Movie S2.

Same layout as Figure 6 but as a movie to illustrate the time evolution.

Movie S3.

Similar to Figure 5 but as a movie to illustrate the time evolution. Shows the relative magnetic field enhancement in the $z = 0$ plane (left) and $y = 0$ plane (right). The black contour lines depict the threshold for the magnetosheath jet detection: $P_{\rm d,x} > 0.5\, P_{\rm d,sw}$. The green lines shows the magnetopause.